This article has been accepted for publication in a future issue of this journal, but has not been fully edited. Content may change prior to final publication.
Citation information: DOI: 10.1109/jlt.2026.3664020, Journal of Lightwave Technology



# Experimental Demonstration of Localization in Bending Eavesdropping Using a Physics-Informed Neural Network

Wenshuai Qin, Xiaoxue Gong, Weigang Hou, Lu Gan, Lei Guo

***Abstract*—This paper proposes a physics-informed neural network (PINN) scheme for localizing bending eavesdropping in coherent optical communication systems. First, we establish a signal transmission model under bending eavesdropping based on the Manakov equations to analyze its impact on physical information such as linear birefringence and nonlinearity. Subsequently, a PINN is developed by incorporating physical information such as linear birefringence and nonlinear effects into a convolutional neural network-bidirectional long short-term memory (CNN-BiLSTM) architecture. To validate the effectiveness of the scheme, we construct an experimental platform for bending eavesdropping localization in an 80 km, 168 Gbps quadrature phase shift keying (QPSK) coherent optical communication system. Polarization data during eavesdropping are collected from nine positions with bending radii of 10.8 mm and 15 mm. The performance of three models, including CNN, CNN-BiLSTM and PINN is evaluated for bending eavesdropping localization under both bending radii. Experimental results demonstrate that the PINN achieves localization accuracies of 100% and 99.8% under bending radii of 10.8 mm and 15 mm, respectively. This work offers a novel theoretical framework and methodological approach for localizing bending eavesdropping in optical fiber communication systems.**

***Index Terms*—Bending eavesdropping localization, physics-informed neural network, secure optical communication.**

## I. Introduction

WITH the advent of the fifth-generation fixed network (F5G) era, optical fibers now carry more than 90% of global internet traffic. In particular, submarine optical cables are responsible for over 99% of intercontinental communications [1]–[6]. Since optical fibers are insulating media with high resistance to electromagnetic interference (EMI) and exhibit near-zero signal leakage during propagation, they were traditionally regarded as secure. However, with the emergence of advanced eavesdropping techniques such as fiber bending, V-groove cutting, grating scattering, beam splitting, and evanescent coupling, researchers have demonstrated that fiber communication systems are highly vulnerable to eavesdropping. Among these, fiber bending eavesdropping has attracted considerable research attention owing to its low implementation cost and high concealment capabilities [7]–[12]. Moreover, because the power level of the eavesdropped signal is generally below the sensitivity threshold of conventional detection equipment, effective localization using existing monitoring systems remains challenging [13]–[15]. Furthermore, with optical transmission rates reaching terabits per second (Tbit/s), even brief instances of bending eavesdropping can lead to substantial data leakage. Hence, the development of effective localization methods for bending eavesdropping is critically important.

Current research on the localization of bending eavesdropping primarily focuses on machine learning (ML) methods [16]–[22]. Khouloud Abdelli et al. [23] proposed an innovative method that integrates a bidirectional gated recurrent unit (BiGRU) algorithm with optical time-domain reflectometry (OTDR) sensing. By analyzing OTDR trace data containing signatures of bending eavesdropping, they achieved an F1 Score of 96.86%. However, the localization performance for weak signals with eavesdropping induced losses below 1 dB requires further validation. Song [24] developed an intelligent localization framework based on the convolutional neural network,that combines eye diagram features with monitoring data, achieving a localization accuracy of 92.76% under a 5% splitting ratio. Ref [25] proposed a clustering based multi-node data linkage scheme that coordinates data from the transmitter, transmission link, and receiver, achieving a single-point localization accuracy of 99.79%. Although these studies have advanced the localization of bending eavesdropping, they lack a theoretical model of the eavesdropping behavior. This makes it difficult to systematically explain the physical mechanisms affecting optical signal transmission. More importantly, current data-driven black-box models fail to incorporate the physical equations governing optical signal transmission under bending eavesdropping. This disconnect between physical principles and data-driven approaches may limit the accuracy and generalization capability of the localization algorithms.

To address these challenges, this paper proposes a physics-informed neural network (PINN) scheme for localizing bending eavesdropping in coherent optical communication systems. First, the transmission of optical signals under bending eavesdropping is modeled using the Manakov equations, which capture the variations in physical information such as linear birefringence and nonlinear effects. Subsequently, by incor-

This work was supported in part by the National Key Research and Development Program of China under Grant 2023YFB2905900, in part by the National Natural Science Foundation of China under Grants U24B20134, 62222103, in part by the Chongqing Municipal Education Commission under Grants KJZD-K202400608.

Wenshuai Qin, Xiaoxue Gong (Corresponding author), Weigang Hou, Lei Guo are with the School of Communications and Information Engineering, Chongqing University of Posts and Telecommunications, Chongqing 400065, China (e-mail: gongxx@cqupt.edu.cn).

Wenshuai Qin, Xiaoxue Gong, Weigang Hou, Lei Guo are with the Institute of Intelligent Communications and Network Security, Chongqing University of Posts and Telecommunications, Chongqing 400065, China.

Lu Gan is with Department of Electrical and Computer Engineering, Brunel University London, UB8 3PH, U.K.

porating physical information including linear birefringence and nonlinear effects into a convolutional neural network-bidirectional long short term memory (CNN-BiLSTM) framework, we develop a PINN model. In PINN, we designed a composite loss function by integrating the Manakov equations as a physical constraint with data-driven optimization methods. Within this function, the Manakov equations serve as a physical regularization term to characterize the evolution of optical signals under bending eavesdropping, while the data-driven term focuses on optimizing network parameters. To validate the effectiveness of the scheme, we construct an experimental platform for bending eavesdropping localization in an 80 km, 168 Gbps quadrature phase shift keying (QPSK) coherent optical communication system. Polarization data during eavesdropping are collected from nine positions with bending radii of 10.8 mm and 15 mm. A comparative analysis involving CNN, CNN-BiLSTM, and the proposed PINN model is conducted to evaluate localization performance under both bending radii. Experimental results demonstrate that the PINN achieves localization accuracies of 100% and 99.8% under bending radii of 10.8 mm and 15 mm, respectively. Our work provides a novel theoretical foundation and methodological framework for localizing bending eavesdropping in optical fiber communication systems.

The remainder of this paper is organized as follows: Section II presents an optical signal transmission model under bending eavesdropping based on the Manakov equations. Section III details the bending eavesdropping localization scheme based on PINN. Section IV describes the experimental setup and bending eavesdropping data collection. Section V presents the experimental results and performance evaluation of the PINN model. Section VI concludes the paper.

## II. Modeling of Optical Signal Transmission and Analysis of Polarization Data under Bending Eavesdropping

### A. Modeling of Bending Eavesdropping via Optical Signal Transmission Based on the Manakov Equations

To investigate the impact of bending eavesdropping on the physical characteristics of optical signal transmission, we develop a dual-polarization coherent optical communication system model based on the Manakov equations [26]. The equations describe the propagation of optical waves in two orthogonal polarization states, with the mathematical formulation as follows:

$$\begin{aligned}&\frac{\partial A_x}{\partial z}+\beta_{1x}\frac{\partial A_x}{\partial t}+\frac{i\beta_2}{2}\frac{\partial^2 A_x}{\partial t^2}+\frac{\alpha}{2}A_x\\&=\frac{i\Delta\beta_x}{2}A_x+\frac{i8\gamma}{9}\left(|A_x|^2+|A_y|^2\right)A_x\end{aligned}\tag{1}$$

$$\begin{aligned}&\frac{\partial A_y}{\partial z}+\beta_{1y}\frac{\partial A_y}{\partial t}+\frac{i\beta_2}{2}\frac{\partial^2 A_y}{\partial t^2}+\frac{\alpha}{2}A_y\\&=\frac{i\Delta\beta_y}{2}A_y+\frac{i8\gamma}{9}\left(|A_y|^2+|A_x|^2\right)A_y\end{aligned}\tag{2}$$

Here, $A_x$ and $A_y$ represent the complex amplitudes of the X and Y polarized components, describing both the amplitude and phase of the dual-polarization signal. The variable $z$ denotes the propagation distance along the fiber, and $t$ is the time variable. $\beta_{1x}$ and $\beta_{1y}$ are the group delays for the X and Y polarization states, while $\beta_2$ represents the group velocity dispersion. $\alpha$ denotes the fiber attenuation coefficient. $\triangle\beta_x$ and $\triangle\beta_y$ indicate the propagation constant mismatch for the X and Y polarization components caused by fiber birefringence. The nonlinear coefficient $\gamma$ characterizes the fiber nonlinear effects.

### B. Linear Birefringence Characteristics Under bending eavesdropping

In a bending eavesdropping scenario, under quasi-continuous wave conditions, the Manakov equations can be simplified to the following form by neglecting the effects of the time derivative term and fiber loss term:

$$\frac{\partial A_x}{\partial z}=\frac{i\Delta\beta_{be,x}}{2}A_x+\frac{i8\gamma_{be}}{9}\left(|A_x|^2+|A_y|^2\right)A_x\tag{3}$$

$$\frac{\partial A_y}{\partial z}=\frac{i\Delta\beta_{be,y}}{2}A_y+\frac{i8\gamma_{be}}{9}\left(|A_y|^2+|A_x|^2\right)A_y\tag{4}$$

By neglecting nonlinear effects ($\gamma=0$) and solving Eq. (3) and Eq. (4) under the assumption of an input optical power $P$, the analytical solution is given by:

$$A_x=\sqrt{P}\cos\left(\frac{1}{2}\Delta\beta_{be,x}z\right)\tag{5}$$

$$A_y=i\sqrt{P}\sin\left(\frac{1}{2}\Delta\beta_{be,y}z\right)\tag{6}$$

Here, $\Delta\beta_{be,x}=2\pi n_{be,x}/\lambda$, $\Delta\beta_{be,y}=2\pi n_{be,y}/\lambda$ represent the propagation constants for the X and Y polarization under bending eavesdropping. $n_{be,x}$ and $n_{be,y}$ are the corresponding effective refractive indices. The differential propagation constant defined as $\Delta\beta_{be}=2\pi/\lambda(n_{be,x}-n_{be,y})$, characterizes the linear birefringence induced by bending eavesdropping. As a result, the X polarization $\sqrt{P}\cos(\Delta\beta_{be,x}z/2)$ exhibits periodic attenuation with increasing birefringence or propagation distance, while the Y polarization power $i\sqrt{P}\sin(\Delta\beta_{be,x}z/2)$ correspondingly shows periodic enhancement. This oscillatory power exchange between the X and Y polarizations provides a distinct signature that can be leveraged for localizing bending eavesdropping

### C. Nonlinear Effects Under bending eavesdropping

When nonlinear effects are considered, the solutions to Eq. (3) and Eq. (4) are given by:

$$A_{x/y}=\left(\frac{9\Delta\beta_{be,x/y}}{8\gamma_{be}}\right)^{1/2}\sqrt{p_{x/y}}\exp\left(i\phi_{be,x/y}\right)\tag{7}$$

in which the nonlinear coefficient under bending eavesdropping $\gamma_{be}$ is defined as:

$$\begin{aligned}\gamma_{be}&=\frac{\omega_0\frac{3\chi^{(3)}_{xxx}}{4\varepsilon_0 c[1+\chi^{(1)}_{xx}]}}{c\frac{\left[\int_{-\infty}^{+\infty}\int_{-\infty}^{+\infty}|F(x,y)^2|d_x d_y\right]^2}{\int_{-\infty}^{+\infty}\int_{-\infty}^{+\infty}|F(x,y)^4|d_x d_y}}=\frac{\omega_0 n_2}{cA_{eff}}\\n_2&=\frac{3\chi^{(3)}_{xxx}}{4\varepsilon_0 c n_{be}^2},\end{aligned}\tag{8}$$

where $\omega_0$ is the central frequency of the optical field. $\mu_0$ and $\varepsilon_0$ denote the magnetic permeability and electric permittivity of vacuum, respectively. $\chi_{xx}^{(1)}$ is the first-order electric susceptibility, which characterizes the fiber linear dispersion properties. $\chi_{xxxx}^{(3)}$ is the third-order electric susceptibility, describing the fiber nonlinear effects. $n_2$ is the nonlinear refractive index coefficient, $A_{eff}$ is the effective mode area, $c$ is the speed of light in vacuum, $F(x, y)$ denotes the transverse distribution function. $n_{be}$ is the refractive index under bending eavesdropping. As indicated by Eq. (7) and Eq. (8), bending eavesdropping affects the nonlinear transmission characteristics of the fiber channel by altering $n_{be}$. Specifically, bending eavesdropping directly affects the nonlinear refractive index coefficient $n_{be}$ by altering $n_2$, thereby influencing $\gamma_{be}$. The resulting changes in $\gamma_{be}$ affect the nonlinear phase evolution of the transmitted signal. These phase modifications introduce distinctive optical signatures, which can be exploited for the localization of bending eavesdropping.

### *D. Polarization Data Analysis Under Bending Eavesdropping*

Building upon the aforementioned theoretical model, bending eavesdropping affects the amplitude and phase of the X and Y polarization components of the optical signals by modifying the linear birefringence and nonlinear coefficients. These variations are reflected in the four-dimensional polarization data (HI, HQ, VI, VQ), which can be mathematically expressed as follows:

$$\begin{aligned} HI &= (HI(t_1), HI(t_2), HI(t_3), \cdots, HI(t_N)) \\ HQ &= (HQ(t_1), HQ(t_2), HQ(t_3), \cdots, HQ(t_N)) \\ VI &= (VI(t_1), VI(t_2), VI(t_3), \cdots, VI(t_N)) \\ VQ &= (VQ(t_1), VQ(t_2), VQ(t_3), \cdots, VQ(t_N)) \end{aligned} \tag{9}$$

Subsequently, we analyze the structure of the four-dimensional polarization data to select a suitable neural network model. Here, $t_{1,2,3\cdots N}$ denotes the time index. HI and HQ represent the in-phase and quadrature components of the horizontally polarized light field, while VI and VQ correspond to the in-phase and quadrature components of the vertically polarized light field. Fig. 1(a) shows the eavesdropping data of the X polarization component at different positions along an 80 km fiber link, with sampling points spaced every 10 km. Fig. 1(b) illustrates the eavesdropping data of the Y polarization component at same conditions. Since the four-dimensional polarization data are synchronously sampled, the same parameters can be applied for feature extraction. CNN effectively extracts spatial features across different polarization dimensions. Furthermore, each polarization dimension is affected by linear birefringence and nonlinear effects, resulting in time-series features with strong local correlations. To capture these temporal dependencies, we employ a BiLSTM network. Its gating mechanism adaptively learns the locally correlated temporal features inherent in the polarization data.

In summary, bending eavesdropping affects the physical properties of optical signal transmission and induces characteristic variations in polarization data. To localize bending eavesdropping, we propose a PINN model that incorporates physical information including linear birefringence and nonlinear effects into a CNN-BiLSTM architecture. This hybrid methodology integrates physical modeling with data-driven learning, enabling automated extraction of eavesdropping related features from polarization data.

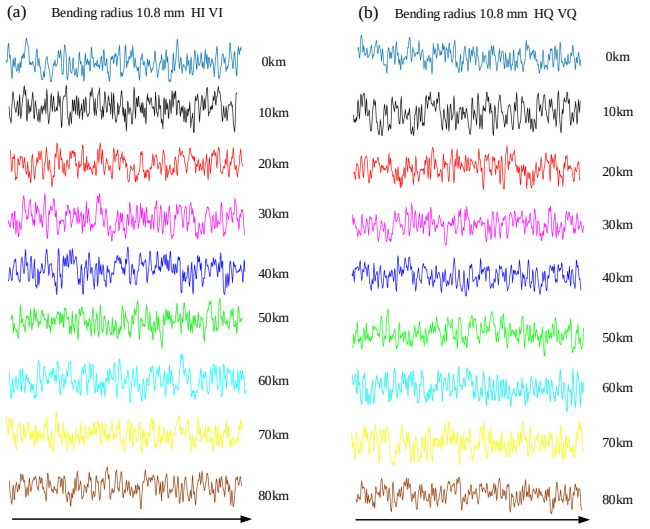


Fig. 1. Bending eavesdropping data collected at nine positions along an 80 km fiber, spaced every 10 km. (a) X polarization component, (b) Y polarization component.

## III. Bending Eavesdropping Localization Scheme

### *A. Overview of the Bending Eavesdropping Localization Scheme*

Fig. 2 illustrates the PINN-based bending eavesdropping localization scheme. The proposed scheme consists of three modules: data collection module, data preprocessing module, and PINN module. In the data collection module, coherent receiver performs optoelectronic conversion to transform optical signals into electrical signals, which are then sampled by an analog-to-digital converter (ADC) to obtain four-dimensional polarization data (HI, HQ, VI, VQ). The data preprocessing module conducts multi-stage processing on HI, HQ, VI, VQ. Data cleaning discards redundant samples and outliers, resampling techniques are employed to balance class distribution, normalization and standardization eliminate scale differences among the features. After preprocessing, the HI, HQ, VI, and VQ data are fed into the PINN module. This module comprises a linear processing layer, a nonlinear processing layer, and a neural network that includes an input layer, multiple hidden layers, and an output layer. The output layer predicts the bending eavesdropping location, labeled as class 0-8. For the loss function design, a dual mechanism combining data-driven and physics constrained approaches is employed, forming a combined loss function incorporating cross-entropy and physical information constraint from the Manakov equations. The cross-entropy loss serves to minimise the discrepancy between the predicted class probability distribution and the ground-truth labels. The residual of the Manakov equations is introduced as a physical information constraint term, thereby constraining

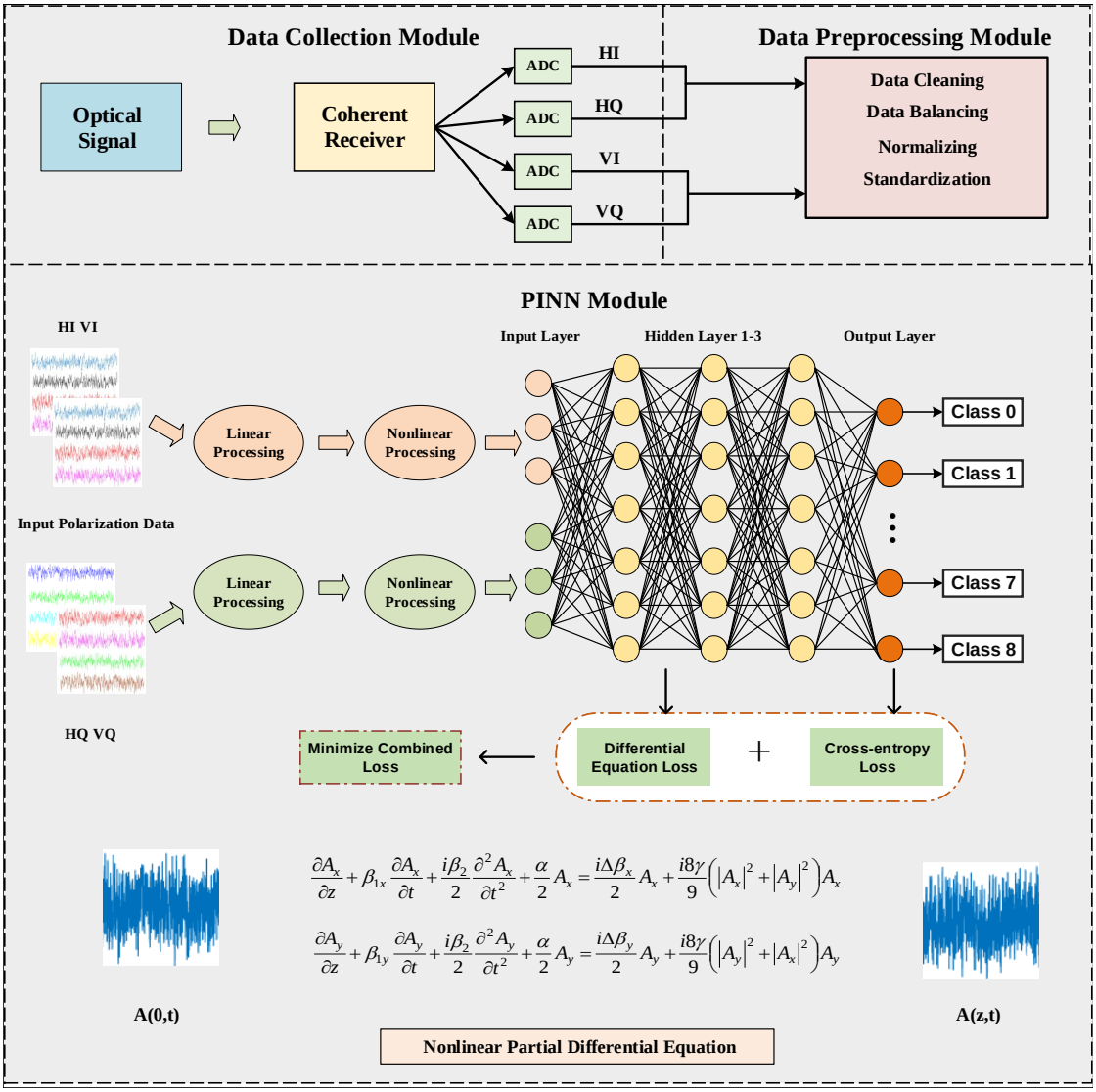


Fig. 2. PINN for bending eavesdropping localization scheme. Data Collection: Coherent receiver performs optoelectronic conversion, followed by ADC sampling to obtain HI, HQ, VI, VQ. Data preprocessing module: Multi-stage processing including data cleaning, data balancing, normalization, and standardization. PINN Module: The processed data are fed into a neural network comprising both linear and nonlinear layers. The output layer predicts the eavesdropping location corresponding to class 0-8

the model outputs to comply with the physical laws governing light transmission. This dual-constraint mechanism has been demonstrated to reduce model prediction errors and enhance the reliability and theoretical rationality of localization results in practical scenarios through its physical information constraint.

### *B. Detailed Architecture of the PINN Model*

In the following section, a comprehensive overview of the PINN model is presented. The architectural design of the model is illustrated in Fig. 3 The HI, HQ, VI, VQ are processed through linear and nonlinear layers to model signal propagation within the optical fiber. Specifically, the linear layer models linear birefringence and dispersion to capture amplitude variations of the signal at different frequencies, while the nonlinear layer accounts for phase variations. The corresponding mathematical formulations are given in Eq. (10) and Eq. (11).

$$X_{R_e} = D_1 \frac{\partial R_e(A)}{\partial t} + D_2 \frac{\partial^2 R_e(A)}{\partial t^2} + c\left(R_e(A) + I_m(A)\right) + N R_e(A)\left(R_e(A^2) + I_m(A^2)\right) \tag{10}$$

$$X_{I_m} = D_1 \frac{\partial I_m(A)}{\partial t} + D_2 \frac{\partial^2 I_m(A)}{\partial t^2} + c\left(I_m(A) + R_e(A)\right) + N I_m(A)\left(R_e(A^2) + I_m(A^2)\right) \tag{11}$$

where $D_1$ and $D_2$ denote dispersion coefficients, $c$ represents linear birefringence, and $N$ corresponds to the nonlinear coefficient. Subsequently, the polarization data are processed by a neural network composed of six convolutional blocks. Each block consists of a convolutional layer, a batch normalization layer, and a max pooling layer. To extract features over a broad range, a convolutional kernel size of $2 \times 5$ is employed.

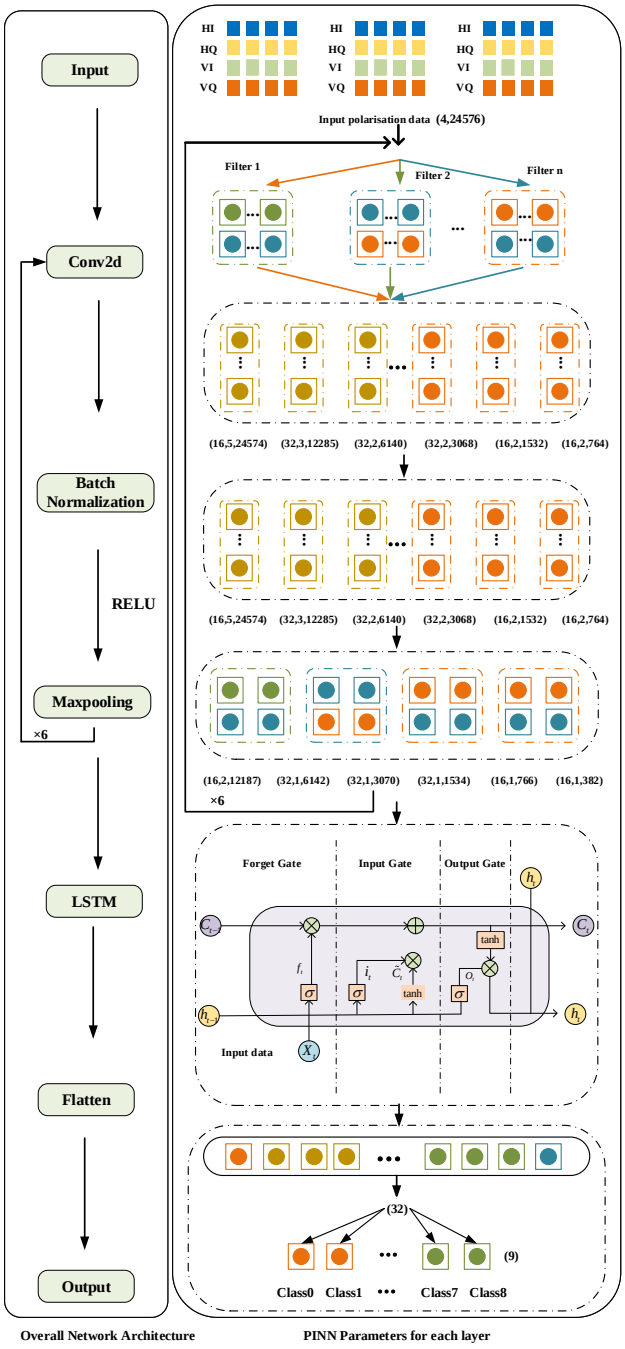


Fig. 3. Architecture and key parameters of the proposed PINN model. CNN: input size $4 \times 24576$, convolutional kernel with size of $2 \times 5$, pooling layer with size of $2 \times 2$, output size $16 \times 1 \times 382$, BiLSTM with 128 units direction, FC layer with $256 \times 9$ parameters for 9 class classification.

Zero-padding is applied to both ends of the input, and the stride is set to 1 to ensure effective feature extraction. The mathematical formulation of the convolutional operation is given by:

$$A_{ij} = \sigma\Big(\sum_{p=0}^{2-1}\sum_{q=0}^{5-1} X_{(i\cdot s+p)(j\cdot s+p)} \cdot W_{pq} + b\Big) \tag{12}$$

where $X$ is the polarization input data, $\sigma$ denotes the activation function, $W$ is the convolutional kernel weight, $b$ is the bias term, and $s$ is the stride. The indices $p$ and $q$ correspond to the vertical and horizontal positions within the kernel, respectively. Specifically, the input to the first convolutional block is polarization data of dimension $4 \times 24576$. This layer employs 16 filters with a kernel size of $2 \times 5$, producing an output of $16 \times 5 \times 24574$. A batch normalization layer is then applied to standardize the output to a zero mean and unit variance. This is followed by a ReLU activation function defined as $Z = \max(0, A_{ij})$. A max-pooling layer then downsamples the feature map by a factor of 2, resulting in an output of $16 \times 2 \times 12187$, which reduces computational complexity while preserving essential features. The pooling operation is defined as:

$$P_{ij} = \max\{Z_{i+m,j+n} \mid 0 \le m < k, 0 \le n < k\} \tag{13}$$

This process is repeated across six convolutional blocks with filter counts set to 16, 32, 32, 32, 16, and 16, respectively. The resulting high-dimensional feature maps are then passed into a BiLSTM module for temporal sequence modeling.

To capture the temporal evolution characteristics of polarization data, the BiLSTM module performs temporal sequence modeling on the extracted feature sequences after CNN. The BiLSTM consists of a single layer with 128 memory units in each direction. The bidirectional outputs are concatenated, resulting in a 256 dimensional hidden state vector at each time step. The final convolutional block of the CNN produces feature maps with dimensions $16 \times 1 \times 382$. Before being fed into the BiLSTM, these features are reshaped into a sequence with two time steps, each containing 6112 features. Each LSTM layer processes a 6112 dimensional input and outputs a 128 dimensional hidden state per direction. These hidden states are then concatenated to form a 256 dimensional feature vector. The concatenated vector is subsequently passed through a fully connected layer consisting of $256 \times 9$ parameters, corresponding to nine output classes.

Finally, the total loss function is is formulated as a combination of the cross-entropy loss and a physical information regularization term, which are jointly optimized during training. The cross-entropy loss quantifies the discrepancy between the predicted probability distribution $p_\theta(y|x)$ and the ground-truth label distribution $q(y|z)$, and is mathematically defined as:

$$\Psi_{CE} = -\sum_{i=1}^{N} q(y_i|x_i) \log p_\theta(y_i|x_i) \tag{14}$$

$N$ denotes the number of sample batches, and $\theta$ represents the trainable parameters. The physical information regularization loss is constructed based on the Manakov equations, and its mathematical expression is expressed as:

$$\Psi^x_{phy} = E[\|\beta_{1be,x}\frac{\partial A_x}{\partial t} + \frac{i\beta_{2be}}{2}\frac{\partial^2 A_x}{\partial t^2} + \frac{i\Delta\beta_{0be,x}}{2}A_x + \frac{i8\gamma_{be}}{9}\left(|A_x|^2 + |A_y|^2\right)A_x\|_x] \tag{15}$$

$$\Psi^y_{phy} = E[\|\beta_{1be,y}\frac{\partial A_y}{\partial t} + \frac{i\beta_{2be}}{2}\frac{\partial^2 A_y}{\partial t^2} + \frac{i\Delta\beta_{0be,y}}{2}A_x + \frac{i8\gamma_{be}}{9}\left(|A_y|^2 + |A_x|^2\right)A_y\|_y] \tag{16}$$

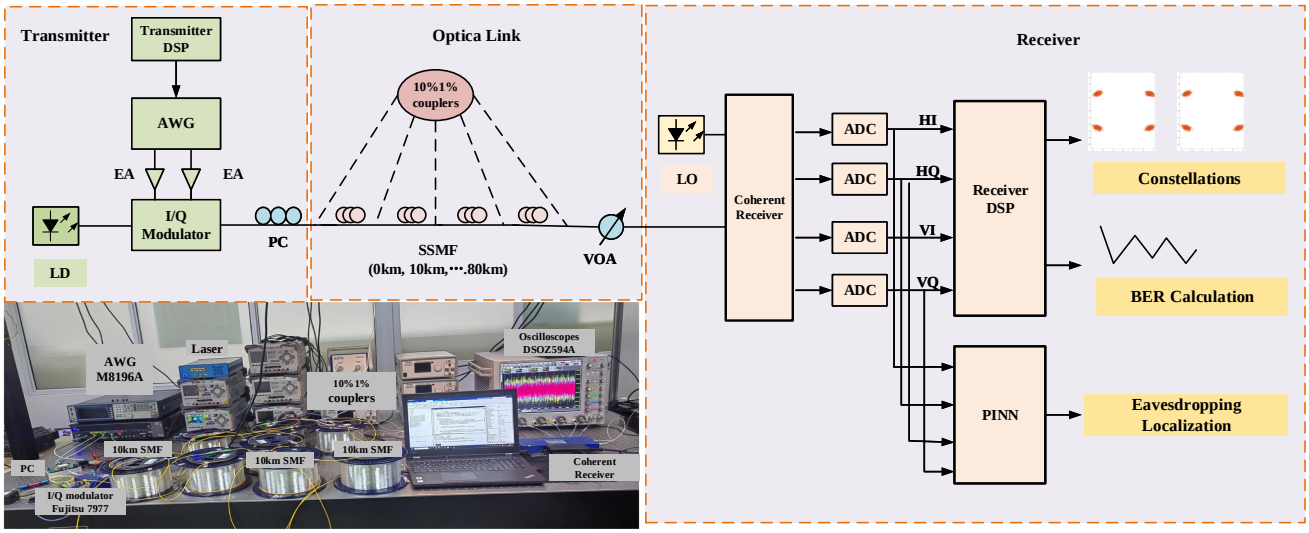


Fig. 4. Experimental step of bending eavesdropping. AWG: Arbitrary waveform generator, LD: Laser diode, EA: Electrical amplifier, IQ-MZM: IQ Mach-Zehnder Modulator, PC: Polarization controller, SSMF: Standard single-mode fiber, VOA: Variable optical attenuator, LO: Local oscillator, PBS: Polarization beam splitter, ADC: Analog-to-digital converter.

The joint optimization objective integrates two loss components, weighted by a tunable parameter $\lambda$. The model is trained using the Adam optimization algorithm, which iteratively updates the parameters by computing the gradients of the total loss function to improve prediction accuracy against the ground truth.

## IV. Experimental Setup and Bending Eavesdropping Data Collection

To validate the feasibility of the PINN based bending eavesdropping localization scheme, an experimental platform is established for an 80 km, 168 Gbps QPSK coherent optical communication systems, as illustrated in Fig. 4. At the transmitter, a pseudorandom binary sequence (PRBS) is generated offline using MATLAB 2022a and fed into an arbitrary waveform generator (AWG, Keysight M8196A) operating at 92 GSa/s to produce 42 GBaud in-phase (I) and quadrature (Q) signals. After amplification by an electrical amplifier (EA, SHF S807C), these signals drive the upper and lower radio frequency (RF) ports of the IQ Mach-Zehnder Modulator (IQ-MZM, Fujitsu FTM7977HQA 8V). A continuous-wave laser diode (LD) with an output power of 10 mW, a linewidth of 100 kHz, and a central frequency of $f_c = 193.415$ THz serves as the optical source. The LD modulates the electrical signals into a QPSK optical signal. A polarization controller dynamically adjusts the polarization state to compensate for transmission disturbances and ensure accurate signal demodulation at the receiver. An 80 km transmission link is established using G.652D single-mode fiber. Based on the theoretical model of bending eavesdropping loss [27], optical couplers with splitting ratios of 10:90 and 1:99 are inserted at intervals of 10 km to simulate bending eavesdropping. These couplers correspond to bending radii of 10.8 mm and 15 mm, respectively. The optical power output is adjusted in real time by a variable optical attenuator (VOA) to ensure signal demodulation.

At the receiver, the optical signal is converted into four electrical signals using a coherent receiver (CPRV1225A U2T). These signals are then digitized by a four-channel oscilloscope (Keysight DSOZ594A) at an 80 GSa/s sampling rate, producing the in-phase (HI) and quadrature (HQ) components of the X polarization, and the in-phase (VI) and quadrature (VQ) components of the Y polarization. The resulting four-dimensional polarization data are subsequently fed into the PINN model for localizing bending eavesdropping. To ensure the transmission performance of the QPSK coherent communication system, offline digital signal processing (DSP) is applied to the digitized signals. The quality of the optical signal is quantitatively evaluated by analyzing the QPSK constellation diagrams and calculating the bit error rate (BER).

For the PINN model dataset, polarization data are collected over an 80 km optical link with bending radii of 10.8 mm and 15 mm. Measurements are taken at nine positions spaced at 10 km intervals. The polarization data corresponding to bending radii of 10.8 mm and 15 mm are compiled into new datasets. Each dataset contains 5940 samples, which are partitioned into training, validation, and test sets with proportions of 6:2:2. The PINN model is implemented, trained, and evaluated using the PyTorch framework.

## V. Results and Analysis

To evaluate the convergence behavior and generalization performance of the PINN model, we analyze accuracy and loss curves on the test sets. Subsequently, we establish a comprehensive quantitative assessment framework based on confusion matrices, from which four key metrics are computed: Accuracy, Precision, Recall, and F1 Score. Finally, we employ t-SNE dimensionality reduction visualization to examine the clustering characteristics of samples from different classes and the decision boundaries. This provides an intuitive demonstration of the model capability in classifying bending eavesdropping features. **Evaluation Metrics:** Model

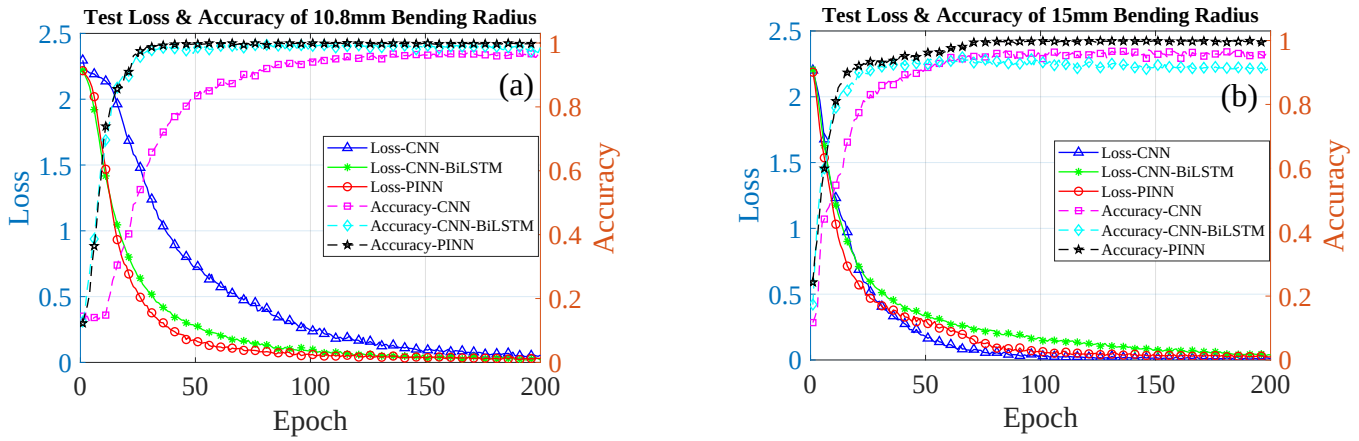


Fig. 5. Training loss and testing accuracy curves of CNN, CNN-BiLSTM, and PINN models under bending eavesdropping. (a) 10.8 mm bending radius, (b) 15 mm bending radius.

performance is quantitatively assessed using four standard classification metrics: *accuracy*, *precision*, *recall*, and *F1 score*. The *accuracy* represents the ratio of correctly predicted samples to the total number of samples:

$$\text{Accuracy} = \frac{\sum_{i=1}^{9} C_{ii}}{\sum_{i=1}^{9}\sum_{j=1}^{9} C_{ij}} \times 100\%. \tag{17}$$

Here, the diagonal elements $C_{ii}$ denote the number of samples whose true class is $i$ and are correctly predicted as class $i$, while the off-diagonal elements $C_{ij}$ correspond to misclassified samples in the confusion matrix.

For each class $k$, the *precision* measures the proportion of correctly predicted samples in class $k$ among all samples predicted as class $k$:

$$\text{Precision}_k = \frac{C_{kk}}{\sum_{j=1}^{9} C_{jk}}. \tag{18}$$

The *recall* quantifies the proportion of correctly predicted samples in class $k$ among all samples that truly belong to class $k$:

$$\text{Recall}_k = \frac{C_{kk}}{\sum_{j=1}^{9} C_{kj}}. \tag{19}$$

Finally, the F1 *score* represents the harmonic mean of precision and recall:

$$\text{F1-Score}_k = 2\,\frac{\text{Precision}_k \times \text{Recall}_k}{\text{Precision}_k + \text{Recall}_k}. \tag{20}$$

### *A. Accuracy and Loss Curve Analysis of the PINN Model for Bending Eavesdropping Localization*

Fig. 5(a) shows the evolution of training loss and testing accuracy over epochs for the CNN, CNN-BiLSTM, and PINN models under a bending radius of 10.8 mm. As training progresses, the loss values for all three models steadily decrease and converge toward zero, indicating effective learning and parameter optimization. Correspondingly, the accuracy of all models increases consistently, demonstrating their strong generalization capability on unseen data. The maximum eavesdropping localization accuracies achieved by the CNN, CNN-BiLSTM, and PINN models are 96.46%, 98.65%, and 100%, respectively.

Fig. 5(b) shows the training loss and testing accuracy over epochs for the CNN, CNN-BiLSTM, and PINN models under bending a radius of 15 mm. All three models exhibit the typical trends of decreasing loss and increasing accuracy. However, their convergence rates are significantly slower compared to those observed at a bending radius of 10.8 mm. The maximum eavesdropping localization accuracies achieved by the CNN, CNN-BiLSTM, and PINN models are 95.03%, 91.25%, and 99.92%, respectively. In summary, the difference in localization accuracy under bending radii of 10.8 mm and 15 mm primarily stems from the decrease in signal leakage power as the bending radius increases. This reduction in leakage weakens the interference to the communication system, making localization via bending eavesdropping considerably more challenging. Furthermore, the high similarity in the distribution of eavesdropped data leads to blurred decision boundaries in classification models, further complicating the localization task. The PINN model effectively captures subtle variations in the eavesdropped signals under bending, demonstrating superior training stability, enhanced generalization capability, and improved classification accuracy.

### *B. Noise Analysis of the Test Set Under Different Bending Radius*

To investigate the impact of Gaussian noise on the classification accuracy of PINN model, we systematically introduce additive noise with standard deviations of 0.05, 0.1, 0.15, and 0.2 to the data set. The results demonstrate a clear inverse relationship between noise intensity and model performance. As the noise level increases, the test accuracy progressively declines. Fig. 6(a) shows the accuracy variation of the proposed PINN model at different noise levels at a 10.8mm bending radius. At noise levels of 0.05 and 0.1, the model accuracy shows only a slight decrease, indicating that the model exhibits a certain degree of robustness to low-intensity

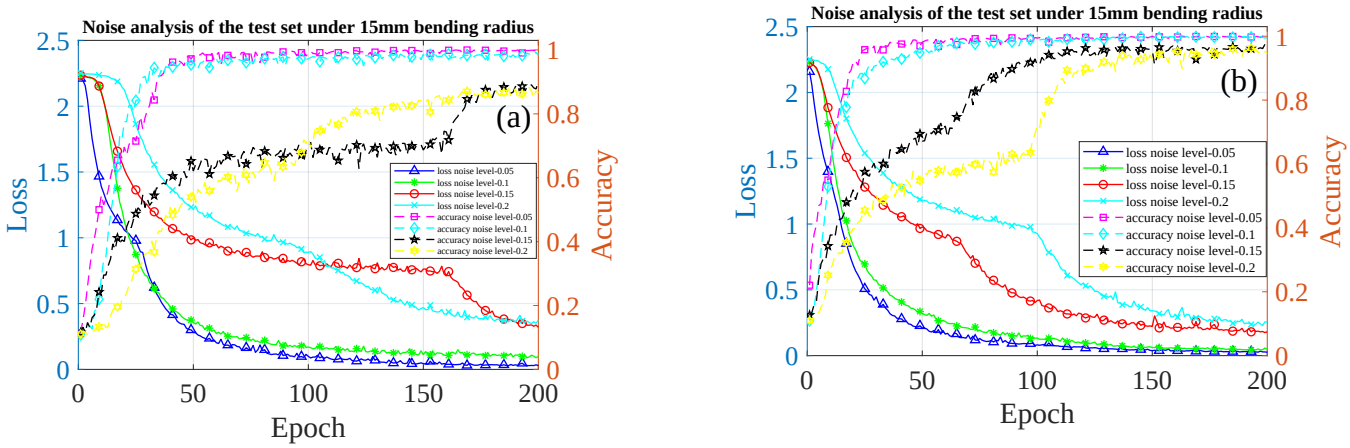


Fig. 6. Noise analysis of the test set under noise level with 0.05, 0.1, 0.15, and 0.2. (a) 10.8 mm bending radius, (b) 15 mm bending radius.

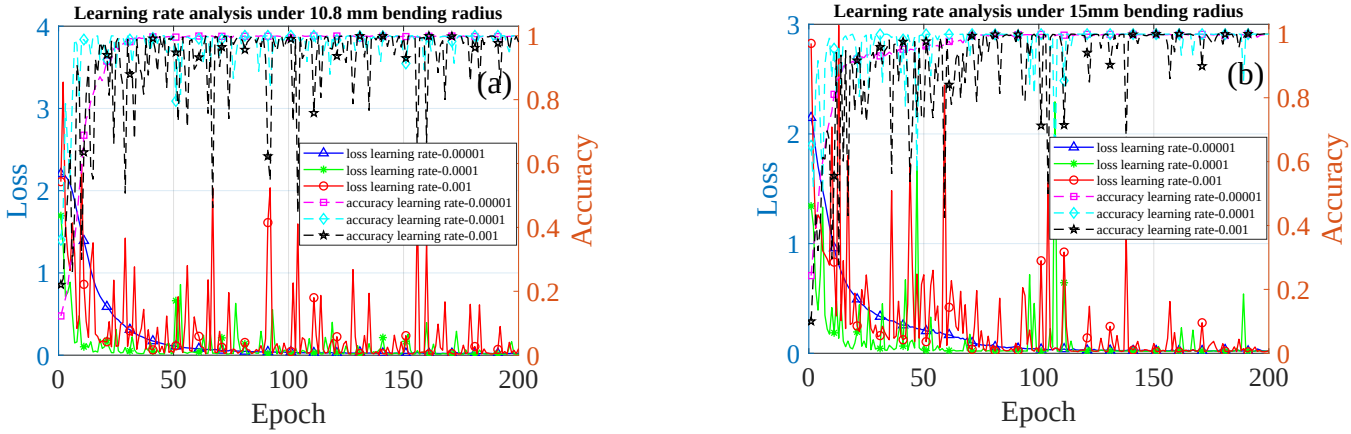


Fig. 7. Learning rate analysis of the under 0.00001, 0.0001, and 0.001. (a) 10.8 mm bending radius, (b) 15 mm bending radius.

noise. However, when the noise standard deviation increased to 0.1 and 0.15, the accuracy showed a significant decline, highlighting the model's vulnerability to strong noise. Fig. 6(b) shows the accuracy variation of the proposed PINN model at different noise levels at a 15 mm bending radius. When the noise standard deviation is 0.05 and 0.1, the model accuracy remains unchanged. When the noise standard deviation is 0.15 and 0.2, the model accuracy shows only a slight decrease, indicating the model's robustness to varying noise intensities. It can be concluded that the PINN model exhibits excellent anti-noise performance and its robustness under 10.8mm and 15mm bending radii.

### *C. Learning Rate Analysis Under Different Bending Radius*

In this section, we systematically investigate the influence of learning rates (0.00001, 0.0001, and 0.001) on the performance of the PINN model. Fig. 7(a) compares the model's performance under different learning rates at a bending radius of 10.8 mm, both accuracy and loss values remain relatively stable throughout the training epochs for learning rates of 0.00001. In contrast, when the learning rate are set to 0.001 and 0.0001, the trends of accuracy and loss exhibit a pronounced deviation from the expected behavior. Fig. 7(b) presents an evaluation under the same settings for a bending radius of 15 mm. The results indicate that with a learning rate of 0.00001, the accuracy and loss of the PINN model continue to demonstrate stable convergence as the number of iterations increases, which aligns with the observations from Fig. 7(a). An excessively high learning rate can cause the optimization process to overshoot the optimal solution, thereby impairing model convergence and introducing greater instability in testing performance. Therefore, the importance of selecting an appropriate learning rate to ensure robust and stable training of the PINN model.

### *D. Performance Metrics Under PINN Model*

Fig. 8(a)-(c) show the confusion matrices for the CNN, CNN-BiLSTM, and PINN models under a bending radius of 10.8 mm. The overall classification accuracies achieved by the three models are 96.4%, 98.6%, and 100%, respectively. Notably, the PINN model achieves perfect classification across all categories, demonstrating exceptional discriminative capability. Fig. 8(d)-(f) present the confusion matrix analysis for the same models when the bending radius increases to 15 mm. Compared with the 10.8 mm case, the classification accuracies of the CNN and CNN-BiLSTM models drop to

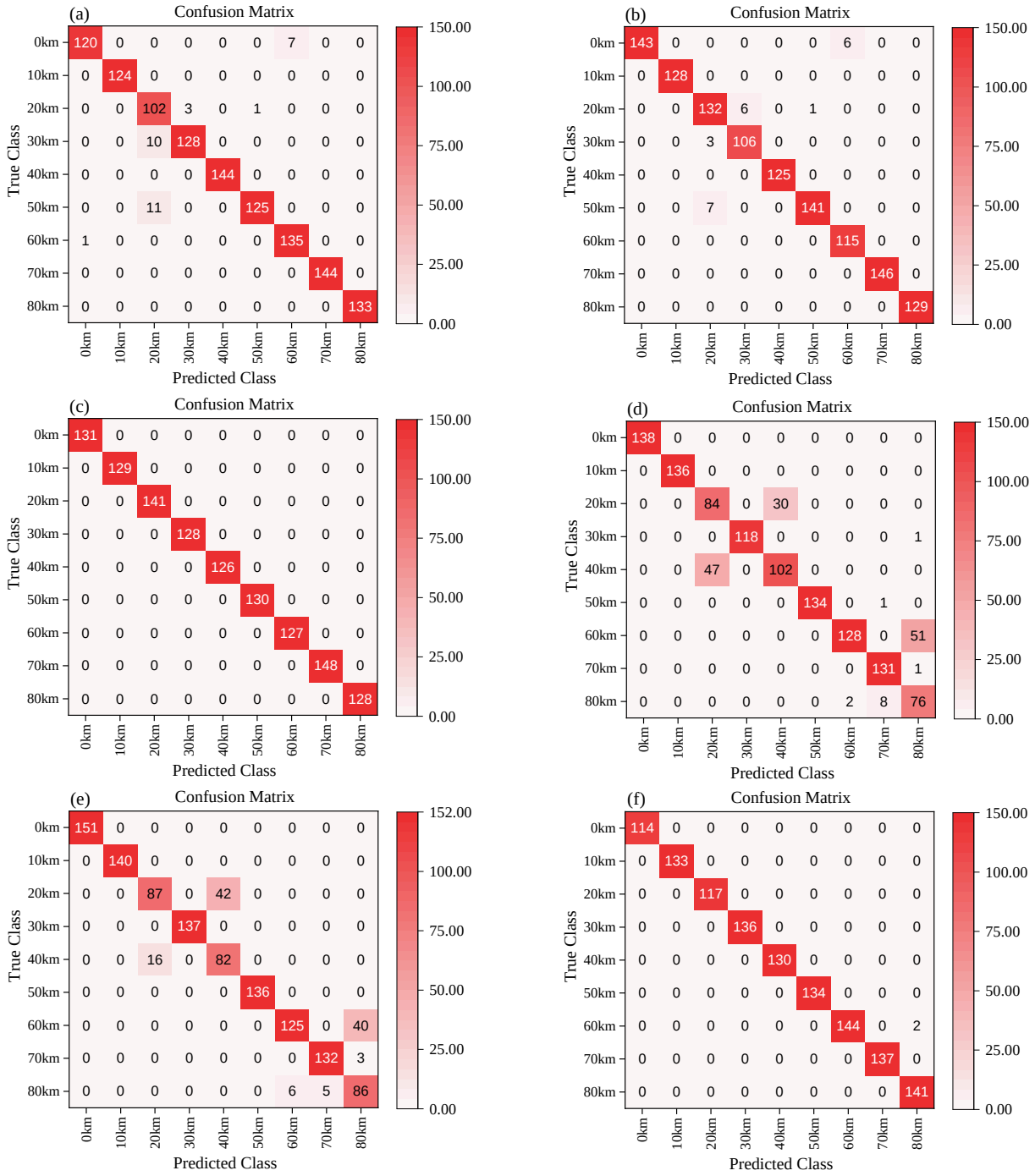


Fig. 8. Confusion matrices of bending eavesdropping localization for CNN, CNN-BiLSTM, and PINN models. (a) CNN-10.8mm bending radius, (b) CNN-BiLSTM-10.8mm bending radius, (c) PINN-10.8mm bending radius, (d) CNN-15mm bending radius, (e) CNN-BiLSTM-15mm bending radius, (f) PINN-15mm bending radius.

95% and 91.2%, respectively. Nevertheless, the PINN model still achieves a classification accuracy of 99.8%, reflecting its strong robustness and superior generalization performance.

Fig. 9(a) presents a comparative analysis of the precision of the CNN, CNN-BiLSTM, and PINN models under a bending radius of 10.8 mm. The PINN model demonstrates a precision of 1.0 across all classes, thereby exhibiting a marked superiority over the CNN and CNN-BiLSTM models, which exhibit average precisions of 0.9641 and 0.9864, respectively. Fig. 9(b) illustrates the precision performance of the three models when the bending radius increases to 15 mm. The PINN model maintains excellent performance with an average precision of 0.9984. Conversely, the average precisions of the CNN and CNN-BiLSTM models drop to 0.9521 and 0.9083, respectively. The CNN model exhibits a pronounced performance degradation at the 80 km location with a significant precision decline. The CNN-BiLSTM model also shows high sensitivity to changes in bending radius, with precisions

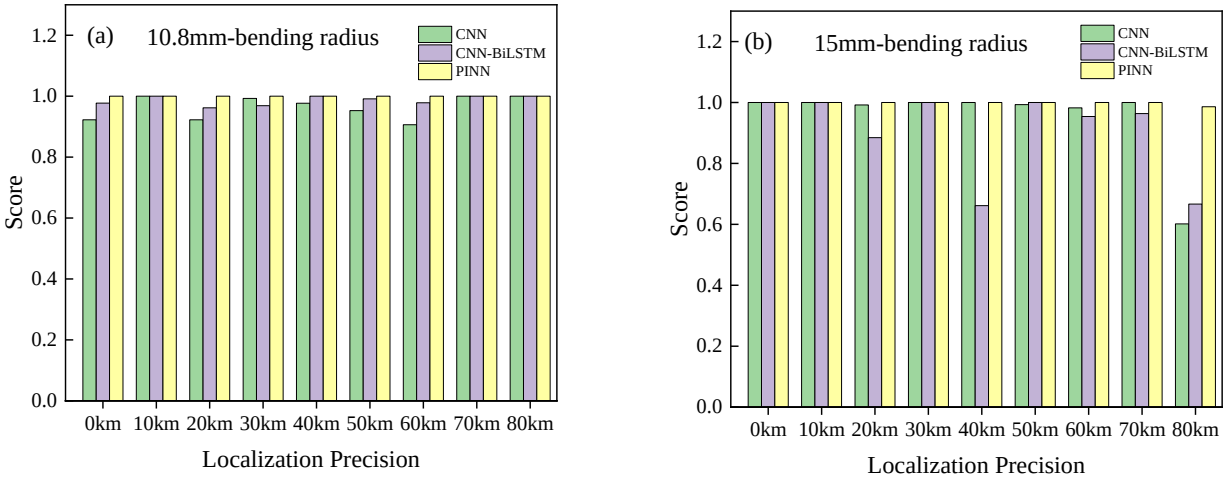


Fig. 9. Precision of CNN, CNN-BiLSTM, and PINN models of nine bending eavesdropping positions. (a) bending radius of 10.8mm, (b) bending radius of 15mm.

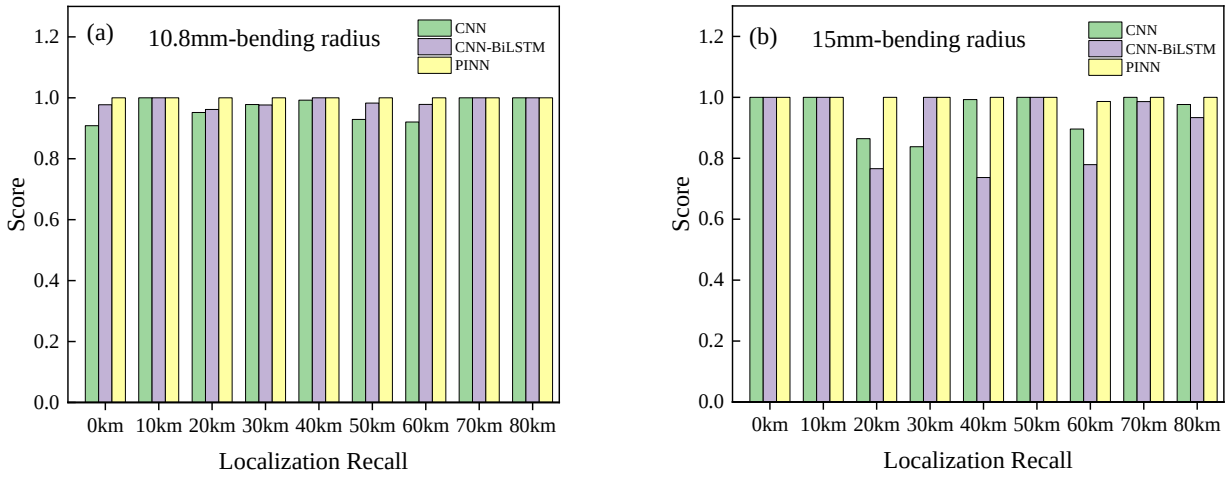


Fig. 10. Recall of CNN, CNN-BiLSTM, and PINN models of nine bending eavesdropping positions. (a) bending radius of 10.8mm, (b) bending radius of 15mm.

dropping to 0.8447, 0.6613, and 0.6667 at the 20 km, 40 km, and 80 km positions, respectively. In summary, the PINN model not only achieves outstanding performance at smaller bending radii but also maintains robust stability and adaptability under more challenging conditions, thus demonstrating its clear superiority in bending eavesdropping localization.

Fig. 10(a) presents the recall of the CNN, CNN-BiLSTM, and PINN models under a bending radius of 10.8 mm. The PINN model maintains a consistent recall rate of 1.0 across the entire range from 0 to 80 km, demonstrating ideal bending eavesdropping localization performance. The CNN model achieves recall rates of 0.9084 and 0.9291 at 0 km and 50 km, while the CNN-LSTM model attains 0.9773 and 0.9828 at the same positions. Fig. 10(b) presents the recall of the CNN, CNN-BiLSTM, and PINN models under a bending radius of 15 mm. The PINN model continues to exhibit excellent robustness, maintaining a recall rate of approximately 1.0 across the entire range from 0 to 80 km, with only a slight decrease to 0.9863 at 60 km. In contrast, the CNN model shows significant performance degradation, with recall rates dropping to 0.8643 at 20 km, 0.8378 at 30 km and 0.8960 at 60 km, reflecting an approximate 11%–17% decline from optimal performance. Although the CNN-BiLSTM model achieves recall rates above 0.98 at 30 km, 50 km and 70 km, it shows significant declines at 20 km and 40 km where the recall rates drop to 0.7658 and 0.7368, indicating performance losses of 21% and 25% relative to the optimal case.

Fig. 11(a) presents a comparative analysis of the F1 Score achieved by the CNN, CNN-BiLSTM, and PINN models under a bending radius of 10.8 mm. The PINN model demonstrates consistent stability across the entire range, maintaining a perfect F1 Score of 1.0 from 0 to 80 km. While the CNN and CNN-BiLSTM models also achieve high performance overall, they exhibit localized performance degradations at specific distances. The CNN model shows slight decreases in F1 Score by approximately 6% to 9% at 0 km, 20 km, 50 km, and 60 km. The CNN-BiLSTM model effectively reduces these degradations to about 2% to 3% by leveraging temporal feature integration through BiLSTM layers. Fig. 11(b) presents a comparative analysis of the F1 Score of the CNN, CNN-

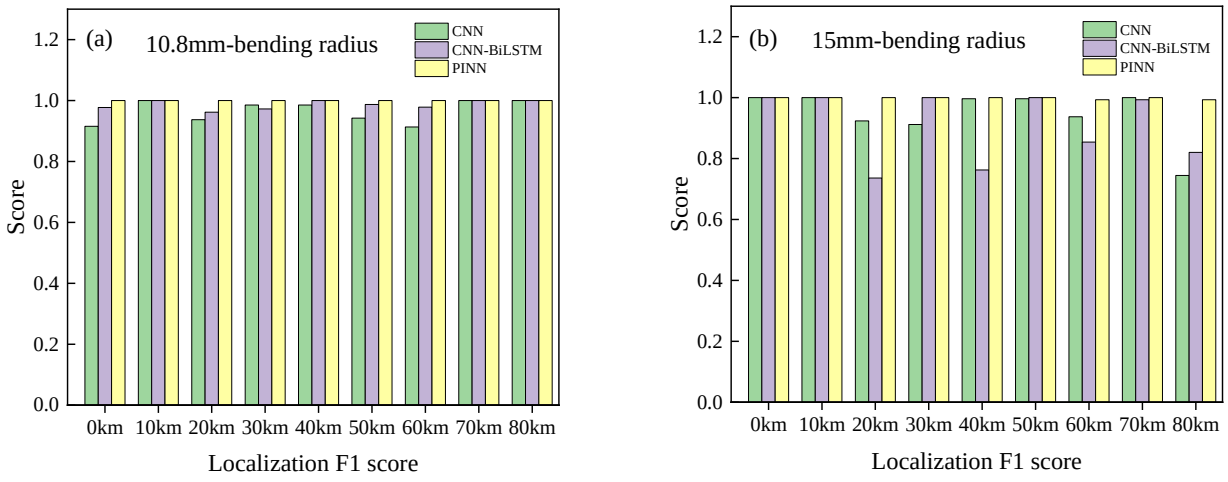


Fig. 11. F1 Score of CNN, CNN-BiLSTM, and PINN models of nine bending eavesdropping positions. (a) bending radius of 10.8mm, (b) bending radius of 15mm.

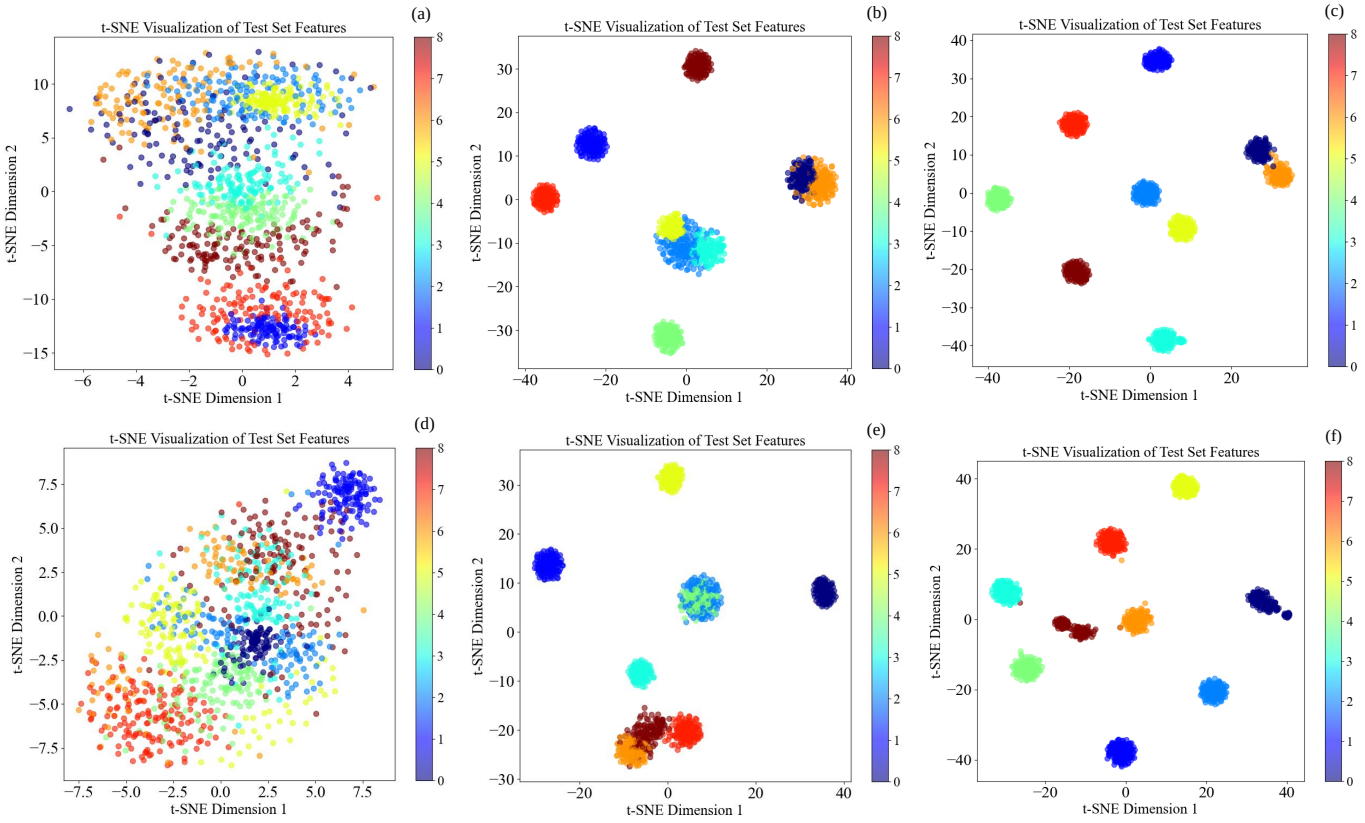


Fig. 12. Feature visualization results based on t-SNE. (a) CNN-10.8mm bending radius, (b) CNN-BiLSTM-10.8mm bending radius, (c) PINN-10.8mm bending radius, (d) CNN-15mm bending radius, (e) CNN-BiLSTM-15mm bending radius, (f) PINN-15mm bending radius.

BiLSTM, and PINN models under a bending radius of 15 mm. The PINN model demonstrates robustness advantage, maintaining a consistently stable F1 Score of 1.0 over the distance range from 0 to 80 km, with only slight deviations observed at 60 km and 80 km. The CNN model suffers a significant F1 Score decrease ranging from 18% to 22% at mid to long distances, such as 30 km and 80 km. Although the CNN-BiLSTM model mitigates some of these declines through temporal modeling, it still experiences performance degradation ranging from 12% to 25% at locations including 20 km, 40 km, 60 km, and 80 km. Quantitative evaluation using metrics such as accuracy, precision, recall, and F1 Score demonstrates the superior performance of the PINN model in bending eavesdropping localization.

To further evaluate the representational differences among various models in bending eavesdropping localization, t-SNE based feature visualization is employed, as shown in Fig. 12. Fig. 12(a) presents the t-SNE visualization of the CNN model

at a bending radius of 10.8 mm. The sample points are widely dispersed with poorly defined class boundaries, indicating considerable inter-class overlap and ambiguity. This performance is attributed to the model's lack of temporal feature modeling, resulting in insufficient spatial feature extraction capability to effectively distinguish between intra-class and inter-class samples. In contrast, the CNN-LSTM model, presented in Fig. 12(b), demonstrates significantly improved decision boundary separability by incorporating temporal features. Nevertheless, some overlap in feature representations persists among certain classes, suggesting room for further enhancement. The PINN hybrid model, which incorporates physical information, demonstrates a clear advantage as illustrated in Fig. 12(c). Fig. 12(d)-(f) present the t-SNE visualization of the CNN, CNN-BiLSTM, and PINN models under a bending radius of 15 mm. The CNN model continues to exhibit significant class overlap, while the CNN-LSTM model demonstrates some overlap near class boundaries. In contrast, the PINN model consistently yields a well-separated and orthogonalized feature space. This stability and consistency across different bending conditions demonstrate the effectiveness of incorporating physical constraints. It significantly enhances the model robustness and generalization capability, offering a more reliable solution for bending eavesdropping localization.

## VI. CONCLUSION

The feasibility of utilizing the PINN model to localize bending eavesdropping in coherent optical communication systems has been experimentally investigated. First, a signal transmission model for bending eavesdropping is developed based on the Manakov equations. Building on this model, a PINN incorporating physical characteristics such as linear birefringence and nonlinear effects is designed. Subsequently, an experimental platform is established using an 80 km, 168 Gbps QPSK coherent optical communication system to collect eavesdropping polarization data at nine positions with bending radii of 10.8 mm and 15 mm, respectively. Using the collected dataset, the localization performance of CNN, CNN-BiLSTM, and PINN models under two bending radii are systematically evaluated using multiple metrics, including confusion matrices, precision, recall, F1 Scores, and t-SNE visualizations. Experimental results demonstrate that the PINN model achieves localization accuracies of 100% and 99.8% for bending radii of 10.8 mm and 15 mm, respectively.

## REFERENCES


[1] X. Gong, Q. Zhang, X. Zhang, R. Xuan, and L. Guo, "Security issues and possible solutions of future-oriented optical access networks for 5g and beyond," *IEEE Communications Magazine*, vol. 59, no. 6, pp. 112–118, 2021.

[2] Q. Zhang, X. Zhang, X. Gong, and L. Guo, "Crosstalk-avoid virtual optical network embedding over elastic optical networks with heterogeneous multi-core fibers," *Journal of Lightwave Technology*, vol. 40, no. 24, pp. 7687–7700, 2022.

[3] W. Liu, Y. Zhao, Y. Li, X. Li, S. Rahman, and J. Zhang, "Segmented protection scheme based on maximum bandwidth sharing in f5g," *Journal of Optical Communications and Networking*, vol. 16, no. 11, pp. 1145–1158, 2024.

[4] Q. Zhang, X. Gong, and L. Guo, "All-optical encryption/decryption of dmpsk signals with key steganography for photonic layer security," *Optics Express*, vol. 31, no. 26, pp. 44 523–44 543, 2023.

[5] D. Zhang, J. Zhu, X. Liu, X. Wu, J. Li, Y. Zeng, X. Si, and H. Li, "Fiber-to-the-room: a key technology for f5g and beyond," *Journal of Optical Communications and Networking*, vol. 15, no. 9, pp. D1–D9, 2023.

[6] X. Li, Y. Liu, Y. Zhao, Y. Li, Z. Li, S. Rahman, and J. Zhang, "End-to-end service provisioning based on extended segment routing in multi-domain optical networks of f5g," *Journal of Optical Communications and Networking*, vol. 14, no. 7, pp. 550–561, 2022.

[7] M. Zafar Iqbal, H. Fathallah, and N. Belhadj, "Optical fiber tapping: Methods and precautions," in *8th International Conference on High-capacity Optical Networks and Emerging Technologies*, 2011, pp. 164–168.

[8] S. Karlsson, M. Andersson, R. Lin, L. Wosinska, and P. Monti, "Detection of abnormal activities on a sm or mm fiber," in *2023 Optical Fiber Communications Conference and Exhibition (OFC)*, 2023, pp. 1–3.

[9] N. Skorin-Kapov, M. Furdek, S. Zsigmond, and L. Wosinska, "Physical-layer security in evolving optical networks," *IEEE Communications Magazine*, vol. 54, no. 8, pp. 110–117, 2016.

[10] S. Karlsson, R. Lin, L. Wosinska, and P. Monti, "Eavesdropping g.652 vs. g.657 fibres: a performance comparison," in *2022 International Conference on Optical Network Design and Modeling (ONDM)*, 2022, pp. 1–3.

[11] V. Spurny, P. Dejdar, A. Tomasov, P. Munster, and T. Horvath, "Eavesdropping vulnerabilities in optical fiber networks: Investigating macro-bending-based attacks using clip-on couplers," in *2023 International Workshop on Fiber Optics on Access Networks (FOAN)*, 2023, pp. 47–51.

[12] K. Shaneman and S. Gray, "Optical network security: technical analysis of fiber tapping mechanisms and methods for detection & prevention," in *IEEE MILCOM 2004. Military Communications Conference, 2004.*, vol. 2, 2004, pp. 711–716.

[13] T. D. Bradley, M. v. d. Hout, B. Kalla, V. v. Vliet, M. Bigot-Astruc, A. A. Correa, P. Sillard, G. Weiner, P. Winzer, and C. Okonkwo, "Fiber eavesdropping using tapers in standard and trench-assisted single-mode fibers," *IEEE Photonics Technology Letters*, vol. 36, no. 15, pp. 953–956, 2024.

[14] T. Uematsu, H. Hirota, T. Kawano, T. Kiyokura, and T. Manabe, "Design of a temporary optical coupler using fiber bending for traffic monitoring," *IEEE Photonics Journal*, vol. 9, no. 6, pp. 1–13, 2017.

[15] K. Noto, T. Uematsu, H. Iida, C. Fukai, and I. Ogushi, "Threshold design in fiber termination identification using local injection and otdr," *Optical Fiber Technology*, vol. 81, p. 103497, 2023.

[16] H. Song, R. Lin, L. Wosinska, P. Monti, Y. Li, and J. Zhang, "Eavesdropping detection and localization in wdm optical system," in *2023 IEEE Future Networks World Forum (FNWF)*, 2023, pp. 1–5.

[17] M. Furdek, C. Natalino, F. Lipp, D. Hock, A. D. Giglio, and M. Schiano, "Machine learning for optical network security monitoring: A practical perspective," *Journal of Lightwave Technology*, vol. 38, no. 11, pp. 2860–2871, 2020.

[18] W. Qin, Q. Zhang, W. Hou, X. Zhang, and X. Gong, "Convolutional neural networks for fiber-bending eavesdropping attacks detection in coherent optical communication systems," in *2024 International Conference on Ubiquitous Communication (Ucom)*, 2024, pp. 342–345.

[19] X. Gong, M. Zhou, Q. Zhang, J. Pang, and L. Guo, "Experimental demonstration of optical eavesdropping detection based on the backpropagation neural network for coherent optical communication systems," in *2022 Asia Communications and Photonics Conference (ACP)*, 2022, pp. 491–494.

[20] Y. Li, Y. Liang, M. Zhang, S. Wei, H. Zhu, Y. Li, Y. Zhao, and J. Zhang, "Fiber eavesdropping detection and location in optical communication system." in *Photonics*, vol. 12, no. 5, 2025.

[21] L. Sadighi, S. Karlsson, C. Natalino, and M. Furdek, "Machine learning-based polarization signature analysis for detection and categorization of eavesdropping and harmful events," in *2024 Optical Fiber Communications Conference and Exhibition (OFC)*, 2024, pp. 1–3.

[22] L. Sadighi, S. Karlsson, C. Natalino, L. Wosinska, M. Ruffini, and M. Furdek, "Deep learning for detection of harmful events in real-world, noisy optical fiber deployments," *Journal of Lightwave Technology*, vol. 43, no. 13, pp. 6092–6101, 2025.

[23] K. Abdelli, J. Y. Cho, F. Azendorf, H. Griesser, C. Tropschug, and S. Pachnicke, "Machine-learning-based anomaly detection in optical fiber monitoring," *Journal of Optical Communications and Networking*, vol. 14, no. 5, pp. 365–375, 2022.

[24] H. Song, Y. Li, M. Liu, K. Wang, J. Li, M. Zhang, Y. Zhao, and J. Zhang, "Experimental study of machine-learning-based detection and location of eavesdropping in end-to-end optical fiber communications," *Optical Fiber Technology*, vol. 68, p. 102669, 2022.

[25] H. Song, R. Lin, L. Wosinska, P. Monti, M. Zhang, Y. Liang, Y. Li, and J. Zhang, "Cluster-based unsupervised method for eavesdropping detection and localization in wdm systems," *Journal of Optical Communications and Networking*, vol. 16, no. 10, pp. F52–F61, 2024.
[26] G. P. Agrawal, *Fiber-optic communication systems*. John Wiley & Sons, 2012.
[27] W. Qin, X. Gong, W. Hou, T. Zhang, X. Zhang, and L. Guo, "Convolutional neural network for detecting fiber-bending eavesdropping attacks in optical communication systems," *Optics Express*, vol. 33, no. 10, pp. 20 894–20 906, 2025.

**Wenshuai Qin** received an M.S. degree in 2021 from Shanxi University, Shanxi, China, where he is currently working toward the Ph.D. degree in Chongqing University of Posts and Telecommunications, Chongqing, China. His research interests include machine learning, fiber nonlinear, optical signal processing, and secure optical transmission system.

**Xiaoxue Gong** (Member, IEEE) received her B.S. degree in 2011, M.S. degree in 2013, and Ph.D. degree in 2017 from Northeastern University, Shenyang, China. During 2016–2017, she conducted academic research at Bangor University, United Kingdom. She is currently a professor in the School of Communication and Information Engineering, Chongqing University of Posts and Telecommunications, China. Her research interests include optical communication, optical signal processing, optical access networks, and network optimization.

**Weigang Hou** (Member, IEEE) received the Ph.D. degree in information and communication system from Northeastern University, Shenyang, China, in 2013. In 2012, he was an Associate Researcher with the Department of Computer Science, City University of Hong Kong, Hong Kong. He is currently a Full Professor with the Chongqing University of Posts and Telecommunications, Chongqing, China. He holds more than 120 publications. Among these, more than 80 papers are published as the first/corresponding author, and they span IEEE magazine, trans, journals, and some famous conferences. His research focuses on the area of optical networks on chips.

**Lu Gan** (Senior Member, IEEE) received the B.Eng. and M.Eng. degrees from South East University, Nanjing, China, in 1998 and 2000, respectively, and the Ph.D. degree from Nanyang Technological University, Singapore, in 2004.,She is currently a Senior Lecturer (Associate Professor) with Brunel University London, Uxbridge, U.K. She has been on the faculties of the University of Newcastle, Callaghan, NSW, Australia, from 2004 to 2006, and the University of Liverpool, Liverpool, U.K, from 2006 to 2007. Her research interests include fundamental signal processing theories and their applications in image/video coding and processing, nondestructive terahertz and ultrasound imaging, machine learning, and wireless communications. Dr. Gan was a Technical Committee Member for conferences, including the IEEE International Conference on Acoustics, Speech and Signal Processing (ICASSP), the IEEE International Conference on Image Processing (ICIP), and Globecom. She is a reviewer for research grants of the Engineering and Physical Sciences Research Council (EPSRC), the Science and Technology Facilities Council (STFC), the Research Foundation Flanders (FWO), and many top journals including IEEE Transactions on Information Theory, IEEE Transactions on Signal Processing, IEEE Transactions on Communications, and IEEE Transactions on Image Processing. She serves as an Associate Editor for the IEEE Signal Processing Letters.

**Lei Guo** (Senior Member, IEEE) received his Ph.D. from the University of Electronic Science and Technology of China in 2006. He is a professor at Chongqing University of Posts and Telecommunications, Chongqing, China. His current research interests include communication networks, optical communications, and wireless communications. He has published over 200 technical papers in the above areas in international journals and conferences, such as the IEEE Transactions on Communications, the IEEE Transactions on Wireless Communications, the IEEE/OPTICA Journal of Lightwave Technology, the IEEE/OPTICA Journal of Optical Communications and Networking, the IEEE GLOBECOM, and the IEEE ICC. He is a member of IEEE and OPTICA, and he is also a senior member of CIC. He is now serving as an editor for five international journals.